RESEARCH ARTICLE

ADVANCED INTELLIGENT SYSTEMS Open Access

www.advintellsyst.com

Symmetry Breaking Metamaterial Sleeve Actuators

*Imran Qayyum Mundial, Alexis Van Merris, Edoardo Milana, and Benjamin Gorissen**

Inflatable soft actuators hold promise for applications that require large and complex deformations. Although they adapt readily to their environment and are inherently safe, they still require a large amount of tethers which limit their applicability. To overcome this limitation, researchers have exploited richness in the energy landscape, expressed in a nonlinear pressure–volume (PV) inflation characteristic, to sequence the motion of multiple actuators with only a few supply lines. However, designing actuators for a certain PV curve is an uphill task. Here, metamaterials, that consist of cylindrically tessellated unit cells, are explored to create a sleeve with nonlinear force–displacement characteristics. When combined with an inflatable core, these metamaterial sleeves imbue nonlinear characteristics to the actuator as a whole, making the PV characteristic tunable via the unit cell's geometry. Where previously, similar architectures were used for shape programming and shape retention, here, the symmetry-breaking properties are analyzed and exploited to create metamaterial sleeve actuators that display a nonreciprocal bending motion; bending to the right during inflation, and to the left during deflation. Finally, the motion nonreciprocity of such actuators is used to make a quadruped robot walk.

1. Introduction

Inflatable actuators are used to drive soft robotic systems[1] as they can achieve complex motions with simple control inputs[2–6] while being safe in interaction with a delicate environment.[7–10] Typically, these actuators have a dedicated pressure supply line to regulate the pressure inside, which is directly linked to the output deformation. Although the actuators can be made compliant and lightweight, the fluidic peripherals, pumps and valves, are typically bulky and stiff. To overcome the limitations of a multitude of tethers, efforts have been directed toward the development of soft and lightweight pumps,[11] and valves[12] that can be integrated in the soft robot's body to produce intricate pressure signals.[13] In general, the number of regulating components increases at best linearly with the number of inflatable actuators. This is a direct consequence of inflatable actuators that have a monotonic pressure–volume (PV) characteristic, where volume is a measure of the overall output deformation of the actuator, and pressure is the regulated input. The number of components in a robot architecture can be decreased by incorporating functionality within the physical characteristics of the actuators, in a paradigm that is referred to as embodied intelligence,[14] physical intelligence,[15] or hardware intelligence.[16] In this paradigm, intelligence is spread throughout the physical structure of the robotic system, rather than localized in a computational unit.[17] Although such intelligence can manifest itself in different forms, it has been shown that for inflatable actuators functionality can be incorporated within the nonlinearities of the PV curve, originating both from material and/or geometry.[18] In our previous work, we made a walking robot by connecting multiple actuators with a peak valley PV curve to a shared pressure supply.[16] Ben-Haim et al. created logic gates using fluid-driven bistable elastic chambers controlled by a single input, where the bistability of the elastic chambers in combination with fluid viscosity enables to program a 5-bit binary output.[19] Milana et al. demonstrated cilia-inspired asymmetric motions using the interconnection of multiple bending actuators with nonlinear peak-valley PV curves.[20] Van Raemdonck et al. developed nonlinear tunable actuators that can generate complicated sequences from a single pressure input by utilizing hysteron features in a cone-shaped actuator, that when combined can play Beethoven's Ninth Symphony with a single pressure supply.[21] Belding et al. preprogrammed a sequence of motions into a serial connection of SLiT (Slit-in-Tube) actuators, by varying the slit geometry.[22] Gorissen et al. made an inflatable soft actuator jump by harnessing the isochoric snapping that of an elastomeric shell, where energy release is encoded in the wave-like shape of the PV curve.[23] However, the design of inflatable actuators for a given nonlinear PV relationship remains an intricate task.

I. Q. Mundial, A. Van Merris, B. Gorissen
Department of Mechanical Engineering
KU Leuven
3001 Leuven, Belgium
E-mail: benjamin.gorissen@kuleuven.be

I. Q. Mundial, A. Van Merris, B. Gorissen
Flanders Make
3001 Leuven, Belgium

E. Milana
Department of Microsystems Engineering
University of Freiburg
79098 Freiburg, Germany

E. Milana
Cluster of Excellence livMatS @ FIT—Freiburg Center for Interactive Materials and Bioinspired Technologies
University of Freiburg
79098 Freiburg, Germany

The ORCID identification number(s) for the author(s) of this article can be found under https://doi.org/10.1002/aisy.202500157.

DOI: 10.1002/aisy.202500157

In the field of mechanical metamaterials, the design of structures for a certain force–displacement (FD) curve is more established. Protocols have been established to shape the global response of mechanical metamaterials, such as inversely designing for auxetic properties[24,25] or FD curves[26] which can also exhibit nonlinearities.[27] Recently, research has been geared to exploit the interaction between nonidentical unit cells, resulting in nonhomogeneous behaviors that can be used to make metamaterials count,[28] and Raney et al. were able to construct mechanical logic gates out of an array of bistable beams and springs, directing the propagation of transition waves.[29] Yang et al. developed a soft, switchable metamaterial with shape-memory and phase-transition properties, by triggering snap-through instabilities using the deflation of internal holes in combination with global compression.[30] In an attempt to merge the fields of mechanical metamaterials and inflatable actuators, Rafsanjani developed a kirigami sleeve around an elongating actuator to make a snake-like soft robot crawl.[31] Jin et al. incorporated the kirigami pattern inside the flexible and inflatable membrane, achieving a certain goal deformation upon inflation,[32] while Sedal et al. achieved similar results by incorporating a planar metamaterial architecture.[33] Rahman et al. exploited multistability in their metamaterial design to create an inflatable actuator that can retain its shape when pressure is removed, harnessing the multistable characteristics in FD space.[34] Here, we will expand upon the concept of merging the field of mechanical metamaterials and inflatable soft robotics and create a metamaterial sleeve by cylindrically tessellating unit cells with nonlinear FD characteristics, imbuing nonlinear characteristics to the global sleeve, as schematically shown in **Figure 1**. Next, we harness the structural nonlinearities of the sleeve to create inflatable actuators with nonlinear PV curves by wrapping such metamaterial sleeves around a soft inflatable central core. The global characteristics of these metamaterial sleeve actuators in the PV domain depend on the unit cell characteristics of the sleeve in the FD domain, giving an avenue to tune its response upon inflation using only geometrical properties. We show that by differentiating the unit cell architecture around the circumference, we create actuators that target a certain deformation sequence, even having the ability to break reciprocity in a single structure. By encoding all functionality in the sleeve of the actuator, a modular design is created where the interchanging of a sleeve leads to new capabilities, as we will demonstrate using a robotic walker.

2. Results

2.1. Unit Cell

To create soft metamaterial sleeve actuators, we start by analyzing the metamaterial's unit cell,[35] which features curved beams with thickness "t" as highlighted in blue in **Figure 2**A. The center line of the curved beams is described by a cosine function with amplitude "$h/2$" and wavelength "L". To concentrate the deformation in the curved beams, we attach them to wide pillars (width "c") that are made out of the same material. The unit cell is completed by a top and bottom beam of height "$c/2$", leaving a gap of "δ" with the rest of the structure. The response of this unit cell, with out-of-plane thickness "T", is analyzed using finite element (FE) analysis, using the commercial package Abaqus. The unit cell structure is discretized using tetrahedral solid elements (C3D20R, C3D15, and C3D10H) using ANSA, a commercial computer-aided engineering software tool. For a mesh refinement study, we refer the reader to SI Section 3.3. The behavior of the material is captured using an incompressible Neo-Hookean material model with an initial shear modulus "G". We loaded the unit cell by encastering the bottom edge and applying a vertical displacement constraint on the top edge of the unit cell using a kinematic coupling, connecting the top edge to a reference point, on which the displacement ("d") is applied. The kinematic coupling allows us to pull the top edge upward while allowing for a rigid body rotation. Furthermore, by monitoring the reaction forces at the reference point as a function of the applied deformation, the FD characteristic is found. To simulate the effect of neighbors, we applied periodic boundary conditions on the left and right edges and restricted out-of-plane movements (see also SI Section 3). All simulations are done using the dynamic implicit method, where we imposed the loading slowly, to capture the quasi-static response. The FD characteristic of a

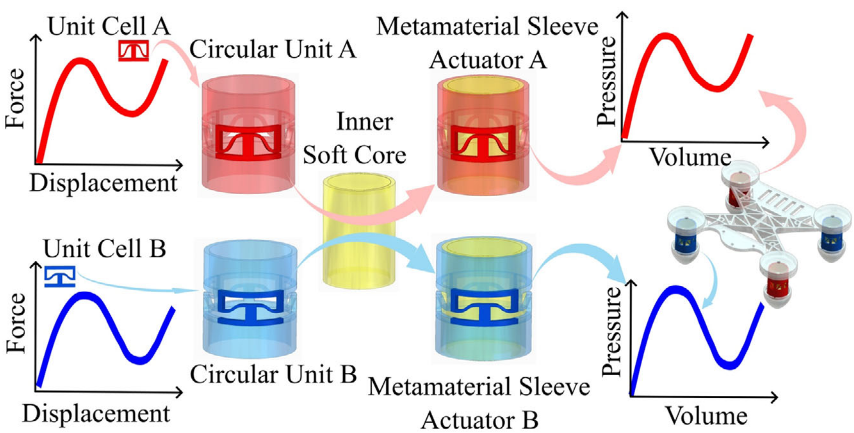

Figure 1. The metamaterial, characterized by a nonlinear FD relationship, influences the linearity of a soft actuator with inherent linear PV behavior, and this nonlinear PV behavior holds potential applications in soft robotics, including functionalities such as sequencing that can aid a robot to walk.

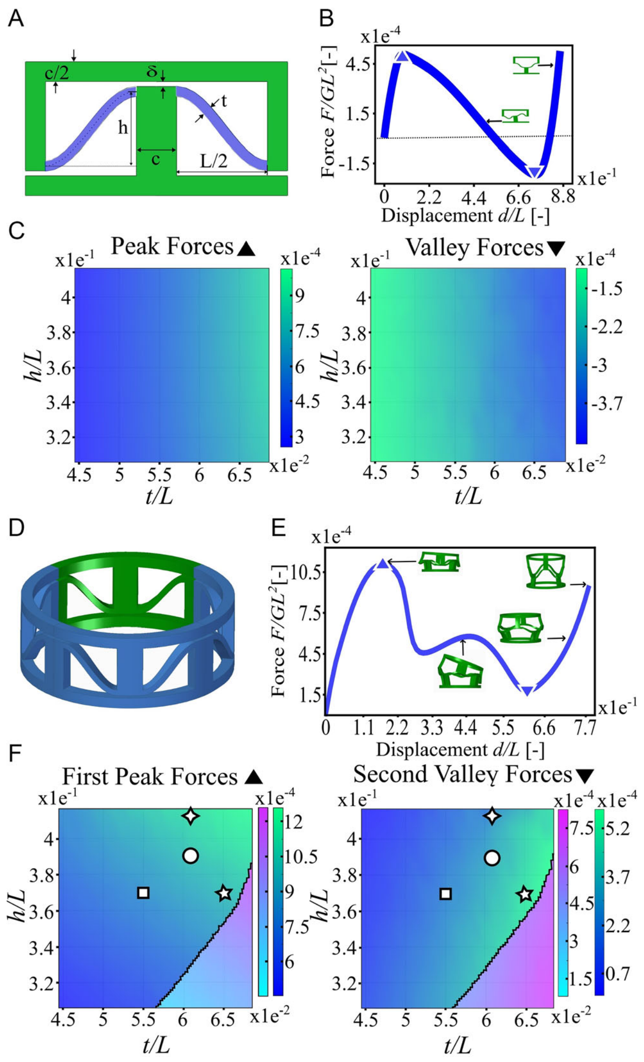

Figure 2. A) A unit cell with defined geometric parameters. B) FD response of a unit cell with peak and valley forces during axial displacement. C) Evolution of peak forces F_p and valley forces F_v as a function of h/L and t/L for unit cells subjected to an axial displacement $D = 16$ mm. D) A cylindrical unit with four metamaterial unit cells. E) FD response for a cylindrical unit with different deformation stages during vertical displacement loading. F) Evolution of the first peak (P_1) and second valley (V_2) forces as a function of h/L and t/L for cylindrical units. The combinations in the bottom right corner feature one peak and one valley highlighted with a distinct color scale.

unit cell with parameters: $t = 1$, $h = 7.5$, $L = 18$, $c = 4$, $\delta = 0.5$, and $T = 1.8$ mm, is displayed in Figure 2B, where we normalized input displacement by the wavelength of the curved beams "L", and reaction force "F" by "GL^2", making the results universal for every rubbery material that follows a Neo-Hookean material model. When pulling the top edge of the unit cell upward, we see that initially, the reaction forces increase until a maximum (indicated by ▲). At this point, the curved beams sequentially buckle, resulting in a zone of negative stiffness, that continues until both beams are inverted, leading to a minimum in reaction force (indicated by ▼). Increasing the displacement further results in the stretching of the beams, with a stiffness similar to the initial loading region. The FD curve shows three zero-crossing points, where two of them are stable, rendering the structure bistable. When loading the structure with force, the response of this unit cell becomes hysteretic, snapping at ▲ when increasing the force input and snapping back when decreasing the force below ▼. In between both force values is a zone where both states (beams curved upward and beams curved downward) are possible and depending on the loading history. As hysteretic behavior is indicative of advanced functionality when having control over the snapping points,[16] we performed a parametric variation study, analyzing the normalized peak force and valley force while varying the geometrical properties of the curved beams, captured by the non-dimensionalized thickness ("t/L"), which is varied between 0.045–0.072, and undulation height ("h/L"), which is varied between 0.3 and 0.42. The results are shown in 2C, where we see that the amplitudes of both peak and valley force are largely dominated by the thickness "t" of the beams. An increase in beam thickness directly leads to both a higher peak force and a lower valley force, giving a single design parameter for tuning the response. The beam height "h" does not contribute significantly to either peak or valley forces. This is in agreement with previous research that showed that peak force scales linearly with normalized height and with the power of four with normalized thickness of the slender beam.[35]

2.2. Uniform Cylindrical Tesselation

As we are interested in creating a sleeve that can enclose an inflatable actuator, we continue our analysis by cylindrically tessellating the proposed unit cell, distributing four units around the circumference, as shown in Figure 2D. We simulate the response of the entire structure by fixing the bottom edge, and linking the displacements of the top edge to the displacement of a single reference point using a kinematic coupling. By doing this we can impose a global upward displacement on the top edge, by imposing a vertical displacement of the reference point, while the top edge is still free to tilt. The FD response of this entire structure is found directly by monitoring the reaction forces on this reference point. When doing this for the same unit cell as before ($t = 1$ $h = 7.5$, $L = 18$, $c = 4$, $\delta = 0.5$, and $T = 1.8$ mm), we see to our surprise a FD curve that has two peaks and two valleys. Initially, the force increases monotonically with displacement, reaching a first peak (indicated by ▲). A further increase in displacement will result in the buckling of some, but not all, of the beams, tilting the structure to one side. The post-buckling behavior of these beams leads to a first zone of negative stiffness, until these beams are everted, resulting in a first force valley. Displacing the structure further will stretch both everted and unbuckled beams, until a point (second force peak) where the remaining beams buckle. This buckling is again followed by a zone of negative stiffness, resulting in a second force valley after which all beams are everted, and the off-axis tilting is restored. The behavior during unloading is analogous as that during loading, following an invariant FD curve. When starting from a fully extended structure (e.g., top right corner of Figure 2E), a decrease in displacement will result in a decrease in force until some, but not all, beams unbuckle (valley force ▼).

Further decrease of displacement will result in the other beams to unbuckle until the structure is fully upright which coincides with the occurrence of the first peak force (▲). This two-peak–two-valley behavior is invariant when the number of unit cells increases, as is further discussed in SI Section 4.1. Although in literature, two-peak–two-valley behaviors have been reported for a serial connection of two single peak-valley structures,[36] the fact that the second peak is lower than the first and the first valley is higher than the second, is indicative of destructive coupling where the buckling of one structure "softens" the other one. The cylindrical tesselation can thus be seen as two hysterons where the snapping of a first hysteron lowers the effort at which the second hysteron snaps.[37] When performing the same parametric variation study as before, we see that both beam thickness "*t*" and amplitude "*h*" influence the global response of the metamaterial sleeve, as shown for the first peak forces and second valley forces on Figure 2F) (full results are detailed in SI Section 3). First, we notice that for a large beam thickness and a low beam height (lower right corner of the design space), the structure only exhibits one peak and valley, and does not exhibit off-axis tilting. This zone is shaded in magenta-cyan, where the color is indicative of the peak and valley force. The green-blue zone corresponds to structures that have two force peaks and two force valleys, where we see that the first peak force increases both with beam thickness and beam height, while the second valley increases with beam thickness but decreases with beam height. Beam height and beam thickness are thus two parameters that can be used to independently tune the first peak and second valley forces. Lastly, we notice that the off-axis tilting direction is determined by imperfections that are present in the mesh and that this tilting direction is conserved during unloading.

2.3. Nonuniform Cylindrical Tesselation

Having demonstrated numerically that the geometrical parameters of the curved beam can be used to tune the nonlinear behavior of a cylindrically tesselated metamaterial sleeve, we now turn our attention to harnessing the symmetry-breaking behavior of uniform metamaterial sleeves to encode motion sequences in nonuniform metamaterial sleeves. As discussed before, the first and last rising branch of the two peak-two valleys FD curve coincides with symmetric deformations, while the first force peak and second force valley delimit a region where symmetry is broken. By combining two types of unit cells in pairs in a single metamaterial sleeve of four unit cells (see **Figure 3**B where type 1 is depicted in red, and type 2 in blue), the relative stacking of the first peak and second valley will determine the global deformation during loading and unloading. We will label the first peak forces by $\blacktriangle_1$ and $\blacktriangle_2$ and the second valley forces by $\blacktriangledown_1$ and $\blacktriangledown_2$ for respectively the first and second type of unit cells. In total, there are thus four different combinations possible: 1) $\blacktriangle_1 > \blacktriangle_2$ & $\blacktriangledown_1 > \blacktriangledown_2$, 2) $\blacktriangle_1 > \blacktriangle_2$ & $\blacktriangledown_1 < \blacktriangledown_2$, 3) $\blacktriangle_1 < \blacktriangle_2$ & $\blacktriangledown_1 < \blacktriangledown_2$, 4) $\blacktriangle_1 < \blacktriangle_2$ & $\blacktriangledown_1 > \blacktriangledown_2$; where combinations 1 and 3, and combinations 2 and 4 are mirror-images of each other. We start by analyzing combination 1 (and thus also combination 3), by simulating the FD curve using the same strategy as described above. For this, we combine two units with $h/L = 0.372$, $t/L = 0.055$

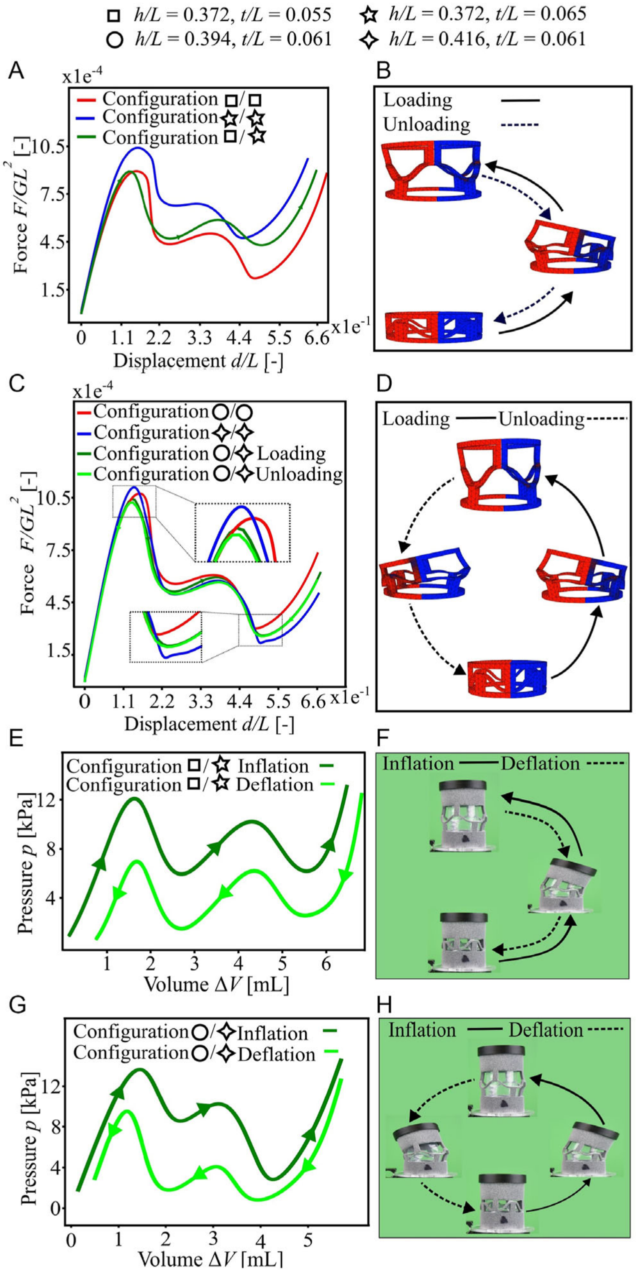

Figure 3. A) Red and blue colors represent the FD relationship for combinations with ■ and ★ symbols, respectively, however, the green color symbolizes the merged cylindrical unit from both combinations. B) The merged cylindrical unit demonstrates symmetric sequencing during the loading/unloading cycle. C) Red and blue colors represent the FD relationship for combinations with ● and ✦ symbols, respectively, however, the green color symbolizes the merged cylindrical unit from both combinations. D) The merged cylindrical unit demonstrates asymmetric sequencing during the loading/unloading cycle. E) PV curve of the merged cylindrical unit performing symmetric sequencing during the inflation/deflation cycle. F) The illustration of the merged cylindrical unit showcasing symmetric sequencing during the inflation/deflation cycle. G) PV curve of the merged cylindrical unit performing asymmetric sequencing during the inflation/deflation cycle. H) The illustration of the merged cylindrical unit showcasing asymmetric sequencing during the inflation/deflation cycle.

(indicated by ■ on Figure 2F) with 2 units with $h/L = 0.372$, $t/L = 0.065$ (indicated by ★). As is shown on Figure 3A, the FD curve of a metamaterial sleeve that only consists of the former units (indicated by ■/■ and in red) has both a lower first peak and second valley as the other (indicated by ★/★ and in blue). The FD curve of the combined structure (indicated by ■/★ and in green) lays in the middle of its parent curves, with a magnitude of its first force peak that corresponds to the one of the red curve, and a magnitude of its second force valley that corresponds to the one of the blue curve. This behavior can be explained by a two-hysteron model[21]: when loading two hysterons in series, the one with the lowest forward snapping threshold (first force peak) will change state first when increasing the effort. During unloading, the hysteron with the highest backward snapping threshold (second force valley) will change state first when decreasing the effort. In our case, this means that during loading the red curved beams will buckle first, and the blue curved beams second. During unloading, the blue curved beams will first revert themselves back to their unbuckled state, and the red curved beams second. In accordance with ref. [16], we will denote the sequence as ■★|★■, where the left side indicates the order during loading, the right side during unloading. Unloading is thus symmetric to loading, which is also reflected in the deformations (see Figure 3B, and Video S1, Supporting Information), that follow the same path during loading and unloading. By programming symmetry breaking in the metamaterial sleeve, we also hardcode the bending direction in the design, whereas previously, this was driven by imperfections. Next, we analyze combination 2 (and thus also combination 4), by combining two units with $h/L = 0.394$, $t/L = 0.061$ (indicated by • on Figure 2F) with 2 units with $h/L = 0.416$, $t/L = 0.061$ (indicated by ✦). As shown on Figure 3C, configuration •/• has a lower first peak force, but a higher second valley force than configuration ✦/✦. As expected from the two hysteron model, during loading • will buckle before ✦, while during unloading • will also revert back before ✦, resulting in a global •✦|•✦ sequence, where loading and unloading are asymmetric. This second symmetry breaking is also apparent in deformation space (see Figure 3D, and Video S1, Supporting Information): during loading the structure tilts to the right, while during unloading, the structure tilts to the left. It thus can be concluded that by spatially varying the units along the circumference, we can program a second form of symmetry breaking in metamaterial sleeves, breaking motion reciprocity.

2.4. Inflatable Actuators

To examine if nonlinear characteristics in the FD domain translate into the PV domain, we fabricate inflatable metamaterial sleeve actuators by 3D printing the cylindrical metamaterial sleeve out of Ultrasint Thermoplastic Polyurethane (90 A-01 - Materialse) with initial shear modulus "G" of 28 MPa, and combining it with a wrinkled low-density polyethylene cylindrical inner membrane with circular laser cut stiffening rings out of PMMA along its length (see also (34) and full details in SI Section 1). In the wrinkled state, the membrane has a low bending stiffness and low pneumatic stiffness (low PV characteristic, see SI Section 2), to not obstruct the intricate deformations of the metamaterial sleeve, and not influence its energy landscape. The inner membrane thus creates an inflatable cavity, and imposes a perpendicular force to the top part of the actuator. Using this method, we create both the symmetric (■/★) and asymmetric (•/✦) designs of Figure 3A,C, and subject them to a volume-controlled inflation test (details in SI Section 2). Both actuators display a characteristic 2 peak - 2 valley PV curve (as shown on Figure 3E,G), which resembles in shape the FD curve of their metamaterial sleeves. Further, the deformations during inflation and deflation also maintain symmetry-breaking properties. The ■/★ actuator exhibits a symmetric ■★|★■ inflation|deflation sequence, tilting to the right during loading and unloading. The •✦ actuator exhibits an asymmetric •✦|•✦ sequence, tilting during to the right during inflation, and to the left during deflation. These deformations can be seen on Figure 3F,H, and on Video S2, Supporting Information, where the inflation is done using air instead of water. From the inflation test, we also notice that the PV curve during loading is substantially higher than the PV curve during unloading. In concordance with,[34] we attribute this to the relaxation of wrinkles in the inner membrane. However, we still see that the general two peak-two valley shape of the PV curve is maintained, together with the (a)symmetric deformation. Finite element analysis also showed that ultimate strains in the structure are well below the yield strain of the material (for details see SI Section 4.2), creating robust actuators that can be integrated in applications.

2.5. Demonstrators

The asymmetric deformation of the developed •✦ actuator is especially interesting as the actuator's tip sweeps an area in deformation space during loading and unloading (see **Figure** 4A). Typically, such loops are the result of an orchestrated actuation of at least two actuatable degrees of freedom,[38] and are exploited by humans for walking,[39,40] and mimicked in conventional bipedal[41] and quadrupedal[42] robots. Inspired by these applications, we exploit the area-sweeping capability of asymmetric metamaterial sleeve actuators to realize a stepping motion when contacting the ground, as shown on Figure 4A. We fabricate four asymmetric actuators with identical characteristics and use them as legs of a quadruped robot (see Figure 4B). Actuators 1 and 3 are diagonally positioned, synchronously inflated, and in anti-phase with actuators 2 and 4 (see Figure 4C). To achieve this, we use a single stepper motor that via a rack and pinion mechanism drives the 4 driving syringes (one for each actuator) simultaneously, where the same stroke that inflates actuators 1 and 3, deflates actuators 2 and 4. In the first instance, we position the robot on a wheeled platform, to minimize the effect of gravitational loading, and see that the robot is able to walk forward in a trotting motion, at a walking speed of 2.5 cm min^{-1}. This reduced speed is a consequence of vertically positioning the legs such that they only touch the ground just before and after full inflation. However, as shown in Figure 4D and in Video S3, Supporting Information, we see that each leg is able to express its full asymmetric stroke. In the second step, we remove the wheeled platform and observe that due to gravitational loading, the actuators are not able to sustain their full stroke (see Video S3, Supporting Information). However, the symmetry-breaking mechanisms of the different actuators are enough to

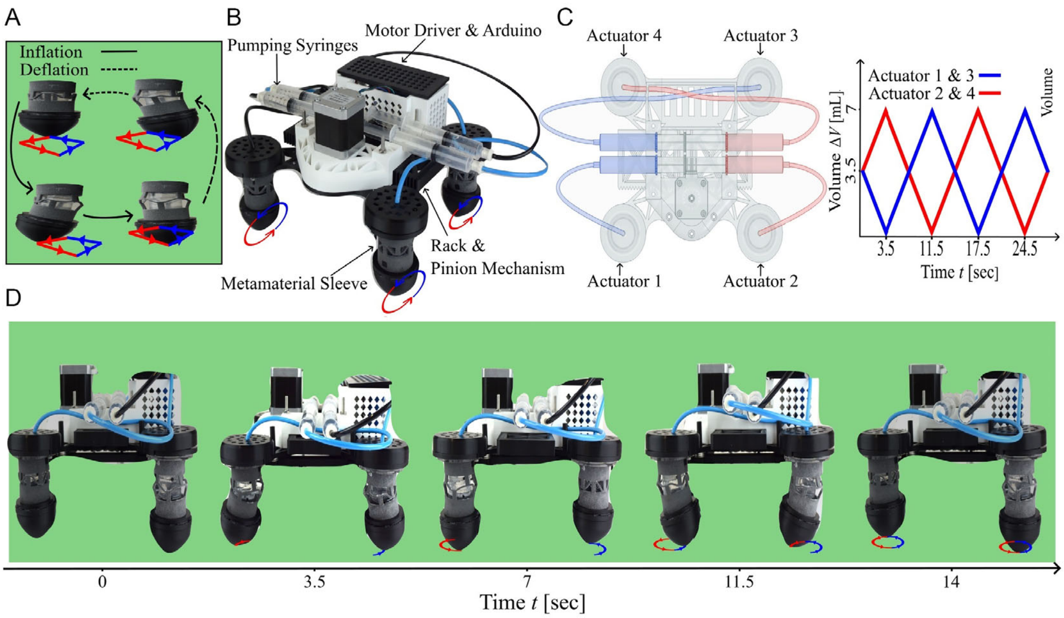

Figure 4. A) Motion trajectory of an asymmetric metamaterial actuator during the inflation/deflation cycle. B) A walking robot with two sets of four fluid-driven asymmetric metamaterial actuators coupled diagonally, driven by four syringe pumps. C) The walking robot's fluidic circuit inflates each set of asymmetric actuators (arranged diagonally), while simultaneously deflating the second set of asymmetric actuators. D) A fluidic circuit controls the motions of each diagonal leg pair for forward walking. The sequence of images from a video of the robot walking using inflation/deflation of the metamaterial sleeve actuators.

break global symmetry and make the robot walk forward, even at a faster walking speed of 82 cm min^{-1}.

3. Conclusion

In summary, we have successfully demonstrated the exploitation of nonlinear metamaterial sleeves to create nonlinear inflatable actuators. We harnessed the spontaneous symmetry breaking in cylindrical metamaterials to create sleeved architectures that can be programmed to exhibit either motion reciprocity or nonreciprocity during loading and unloading. Moreover, by integrating such metamaterial sleeves around an inflatable core, we created metamaterial sleeve actuators with nonlinear PV characteristics that originate solely from the nonlinear FD characteristics of the metamaterial sleeves. These actuators display either symmetric or asymmetric motion sequences during inflation and deflation, where the latter type is especially interesting as the tip of the actuator describes an enclosed area during cyclic loading. This unique feature is exploited to make a robot walk at a walking speed of 2.5 (assisted) and 82 cm min^{-1} (unassisted), where four asymmetric actuators are loaded using a reciprocal input motion. In this research, we focused on the cylindrical tesselation of four unit cells, with results that translate to tesselating more unit cells around the circumference.

In contrast to previous research[16,43] where flow restrictors are used to create asymmetric motions that are dictated by the dynamics of the input signal, the presented solution enables quasi-static sequencing, where even slow walking speeds can be achieved. Further, previous research[19,21,36] showed that actuators with peak-valley PV curves can be sequenced, opening avenues to orchestrate the motion sequence of multiple serially connected metamaterial sleeve actuators. In this respect, we also see the potential to manufacture metamaterial units out of functional materials such that their thresholds can be tuned by external influences, such as temperature,[44] humidity,[45] brightness of the environment,[46] external magnetic fields,[47] or by the dynamics of the input signal.[48] In addition, future work can be directed toward the optimization of the geometrical parameters toward designs that maximize stride length for walking robots, or swept area for swimming robots,[38] Finally, we also see opportunities to incorporate other metamaterial designs in the sleeve, which can lead to other—besides bending—deformation modes.

Supporting Information

Supporting Information is available from the Wiley Online Library or from the author.

Acknowledgements

This research was supported by the Fund for Scientific Research- Flanders (FWO), the European Research Council (ERC starting grant ILUMIS), and the Higher Education Commission (HEC) of Pakistan. E.M. acknowledges additional funding by the Deutsche Forschungsgemeinschaft (DFG, German Research Foundation) under Germany's Excellence Strategy-EXC-2193/1-390951807.

Conflict of Interest

The authors declare no conflict of interest.

Author Contributions

Imran Qayyum Mundial: conceptualization (lead); formal analysis (lead); investigation (lead); methodology (lead); software (lead); visualization (lead); writing—original draft (equal). **Alexis Van Merris**: conceptualization (supporting); formal analysis (supporting); investigation (supporting). **Edoardo Milana**: conceptualization (supporting); supervision (supporting). **Benjamin Gorissen**: conceptualization (supporting); formal analysis (supporting); funding acquisition (lead); methodology (supporting); resources (lead); writing—original draft (equal).

Data Availability Statement

The data that support the findings of this study are available from the corresponding author upon reasonable request.

Keywords

metamaterials, nonlinearity, sequencing, soft robotics, soft sleeve

Received: February 7, 2025
Revised: April 1, 2025
Published online:

[1] B. Gorissen, D. Reynaerts, S. Konishi, K. Yoshida, J.-W. Kim, M. De Volder, *Adv. Mater.* **2017**, *29*, 1604977.
[2] R. Baines, S. K. Patiballa, B. Gorissen, K. Bertoldi, R. Kramer-Bottiglio, *Adv. Mater.* **2023**, *35*, 2300535.
[3] E. Siefert, M. Warner, *Proc. R. Soc. A* **2020**, *476*, 20200047.
[4] T. Gao, J. Bico, B. Roman, *Science* **2023**, *381*, 862.
[5] W. Zhao, Y. Zhang, K. M. Lim, L. Yang, N. Wang, L. Peng, *Mech. Adv. Mater. Struct.* **2024**, 1.
[6] E. W. Hawkes, L. H. Blumenschein, J. D. Greer, A. M. Okamura, *Sci. Rob.* **2017**, *2*, eaan3028.
[7] D. Hutmacher, B. Gorissen, S. Liponsky, T. Shabab, *Multifunct. Mater.* **2021**, *4*, 045001.
[8] Z. Zhang, Y. Long, G. Chen, Q. Wu, H. Wang, H. Jiang, *Sci. Adv.* **2023**, *9*, eadg1203.
[9] J. Shintake, V. Cacucciolo, D. Floreano, H. Shea, *Adv. Mater.* **2018**, *30*, 1707035.
[10] D. Drotman, M. Ishida, S. Jadhav, M. T. Tolley, *IEEE/ASME Trans. Mechatron.* **2018**, *24*, 78.
[11] V. Cacucciolo, J. Shintake, Y. Kuwajima, S. Maeda, D. Floreano, H. Shea, *Nature* **2019**, *572*, 516.
[12] A. M. Moran, V. T. Vo, K. J. McDonald, P. Sultania, E. Langenbrunner, J. H. V. Chong, A. Naik, L. Kinnicutt, J. Li, T. Ranzani, *Commun. Eng.* **2024**, *3*, 117.
[13] S. Hoang, K. Karydis, P. Brisk, W. H. Grover, *PLoS One* **2021**, *16*, e0254524.
[14] R. Pfeifer, *How the Body Shapes the Way We Think: A New View of Intelligence*, MIT Press, Cambridge, USA **2006**.
[15] D. J. Preston, P. Rothemund, H. J. Jiang, M. P. Nemitz, J. Rawson, Z. Suo, G. M. Whitesides. *Proc. Natl. Acad. Sci.* **2019**, *116*, 7750.
[16] B. Gorissen, E. Milana, A. Baeyens, E. Broeders, J. Christiaens, K. Collin, D. Reynaerts, M. De Volder, *Adv. Mater.* **2019**, *31*, 1804598.
[17] C. A. Aubin, B. Gorissen, E. Milana, P. R. Buskohl, N. Lazarus, G. A. Slipher, C. Keplinger, J. Bongard, F. Iida, J. A. Lewis, R. F. Shepherd, *Nature* **2022**, *602*, 393.
[18] D. M. Kochmann, K. Bertoldi, *Appl. Mech. Rev.* **2017**, *69*, 050801.
[19] E. Ben-Haim, L. Salem, Y. Or, A. D. Gat, *Soft Rob.* **2020**, *7*, 259.
[20] E. Milana, B. Van Raemdonck, A. S. Casla, M. De Volder, D. Reynaerts, B. Gorissen, *Front. Rob. AI* **2022**, *8*, 788067.
[21] B. Van Raemdonck, E. Milana, M. De Volder, D. Reynaerts, B. Gorissen, *Adv. Mater.* **2023**, *35*, 2301487.
[22] L. Belding, B. Baytekin, H. T. Baytekin, P. Rothemund, M. S. Verma, A. Nemiroski, D. Sameoto, B. A. Grzybowski, G. M. Whitesides, *Adv. Mater.* **2018**, *30*, 1704446.
[23] B. Gorissen, D. Melancon, N. Vasios, M. Torbati, K. Bertoldi, *Sci. Rob.* **2020**, *5*, eabb1967.
[24] S. Rezaei, J. Kadkhodapour, R. Hamzehei, B. Taherkhani, A. P. Anaraki, S. Dariushi, *Photonics Nanostruct.- Fundam. Appl.* **2021**, *43*, 100868.
[25] X. Zheng, T.-T. Chen, X. Guo, S. Samitsu, I. Watanabe, *Mater. Des.* **2021**, *211*, 110178.
[26] Q. Zeng, Z. Zhao, H. Lei, P. Wang, *Int. J. Mech. Sci.* **2023**, *240*, 107920.
[27] B. Deng, A. Zareei, X. Ding, J. C. Weaver, C. H. Rycroft, K. Bertoldi, *Adv. Mater.* **2022**, *34*, 2206238.
[28] L. J. Kwakernaak, M. van Hecke, *Phys. Rev. Lett.* **2023**, *130*, 268204.
[29] J. R. Raney, N. Nadkarni, C. Daraio, D. M. Kochmann, J. A. Lewis, K. Bertoldi, *Proc. Natl. Acad. Sci.* **2016**, *113*, 9722.
[30] D. Yang, L. Jin, R. V. Martinez, K. Bertoldi, G. M. Whitesides, Z. Suo, *Extreme Mech. Lett.* **2016**, *6*, 1.
[31] A. Parvaresh, B. Seyidoglu, A. Rafsanjani, in *2024 IEEE 7th Int. Conf. on Soft Robotics (RoboSoft)*, IEEE, San Diego, CA **2024**, pp. 519–524.
[32] L. Jin, A. E. Forte, B. Deng, A. Rafsanjani, K. Bertoldi, *Adv. Mater.* **2020**, *32*, 2001863.
[33] A. Sedal, A. H. Memar, T. Liu, Y. Menguc, N. Corson, *IEEE Rob. Automation Lett.* **2020**, *5*, 2272.
[34] S. Rahman, L. Wu, A. El Elmi, D. Pasini, *Adv. Funct. Mater.* **2023**, *33*, 2304151.
[35] D. Restrepo, N. D. Mankame, P. D. Zavattieri, *Extreme Mech. Lett.* **2015**, *4*, 52.
[36] J. T. B. Overvelde, T. Kloek, J. J. A. D'haen, K. Bertoldi, *Proc. Natl. Acad. Sci.* **2015**, *112*, 10863.
[37] J. Liu, M. Teunisse, G. Korovin, I. R. Vermaire, L. Jin, H. Bense, M. van Hecke, *Proc. Natl. Acad. Sci.* **2024**, *121*, e2308414121.
[38] E. Milana, R. Zhang, M. R. Vetrano, S. Peerlinck, M. De Volder, P. R. Onck, D. Reynaerts, B. Gorissen, *Sci. Adv.* **2020**, *6*, eabd2508.
[39] M. S. Nixon, T. Tan, R. Chellappa, *Human Identification Based on Gait*, Vol. *4*, Springer Science & Business Media, New York, NY **2010**.
[40] C. Wan, L. Wang, V. V. Phoha, *ACM Comput. Surv. CSUR* **2018**, *51*, 1.
[41] Y. Sakagami, R. Watanabe, C. Aoyama, S. Matsunaga, N. Higaki, K. Fujimura, in *IEEE/RSJ Int. Conf. on Intelligent Robots and Systems*, Vol. *3*, IEEE, Lausanne, Switzerland **2002**, pp. 2478–2483.
[42] A. T. Sprowitz, A. Tuleu, M. Ajallooeian, M. Vespignani, R. Mockel, P. Eckert, M. D'Haene, J. Degrave, A. Nordmann, B. Schrauwen, J. Steil, A. J. Ijspeert, *Front. Rob. AI* **2018**, *5*, 67.
[43] N. Vasios, A. J. Gross, S. Soifer, J. T. B. Overvelde, K. Bertoldi, *Soft Rob.* **2020**, *7*, 1.
[44] A. Kotikian, C. McMahan, E. C. Davidson, J. M. Muhammad, R. D. Weeks, C. Daraio, J. A. Lewis, *Sci. Rob.* **2019**, *4*, eaax7044.
[45] M. D. N. I. Shiblee, K. Ahmed, M. Kawakami, H. Furukawa, *Adv. Mater. Technol.* **2019**, *4*, 1900071.
[46] S. Li, M. M. Lerch, J. T. Waters, B. Deng, R. S. Martens, Y. Yao, D. Y. Kim, K. Bertoldi, A. Grinthal, A. C. Balazs, J. Aizenberg, *Nature* **2022**, *605*, 76.
[47] W. Hu, G. Z. Lum, M. Mastrangeli, M. Sitti, *Nature* **2018**, *554*, 81.
[48] A. Bossart, D. M. J. Dykstra, J. Van der Laan, C. Coulais, *Proc. Natl. Acad. Sci.* **2021**, *118*, e2018610118.

Supplementary Materials

Symmetry Breaking Metamaterial Sleeve Actuators

Imran Qayyum Mundial, Alexis Van Merris,Edoardo Milana, Benjamin Gorissen

E-mail: Benjamin.Gorissen@kuleuven.be

This PDF file includes:

Supplementary text
Figs. S1 to S10

Supporting Information Text

S1. Fabrication

This section describes the fabrication of the metamaterial sleeve actuator.

S1.1. Inner soft core.

We fabricated an inner soft core with a height of 72 mm and a diameter of 24.6 mm. Specifically, our inner soft core is fabricated using the following nine steps (see Fig S1).

- **Step 1:** The ring with outer threads (inner diameter - 24.6 mm), along with the top and bottom caps is 3D printed using PLA material. The top and bottom caps (diameter - 24.55 mm) are designed with defined cross-patterns to aid in the fitment of the soft core inside of a metamaterial sleeve.
- **Step 2:** We used a laser to cut the stiffener rings out of an acrylic sheet (2 mm) with inner and outer diameters of 22.5 and 24.5 mm respectively.
- **Step 3:** From a transparent LPDE tabular film roll we cut a 72 mm piece for the inner soft core.
- **Step 4:** We glued a 4 mm plastic tube to the bottom cap.
- **Step 5:** We insert the bottom cap in the already-cut LPDE piece (step 5a). We fixed the bottom cap by applying super glue around the circumference and securely holding the bottom cap in place for 15 seconds to ensure proper bonding (step 5b).
- **Step 6:** We insert two stiffener rings at an equal distance in the same LPDE piece (step 6a). We fix the stiffener rings by applying super glue around the circumference and securely holding them in place for 15 seconds to ensure proper bonding (step 6b).
- **Step 7:** We closed this LPDE piece with the top cap at a distance of 52 mm from the bottom cap.
- **Step 8:** We firmly positioned the 3D printed rings on the top and bottom caps (step 7a). We fixed the rings by applying super glue around the circumference and securely holding them in place for 15 seconds to ensure proper bonding (step 8b).
- **Step 9:** We used Smooth-On SIL-POXY silicon glue around the top and bottom caps to prevent leaks.

S1.2. Metamaterial sleeve.

The cylindrical metamaterial sleeve is made of Ultrasint Thermoplastic Polyurethane (TPU) 90A-01 from Materialise (firm). The following steps are employed to make the sleeve fully operational when combined with a soft inner core. (see Fig S2)

- **Step 1:** The rings with inner thread (outer diameter - 29.5 mm) are 3D printed using PLA material.
- **Step 2:** We placed both rings inside the metamaterial sleeve positioning one at the top and the other at the bottom.
- **Step 3:** We fixed the rings by applying super glue around the circumference and securely holding them in place for 15 seconds to ensure proper bonding.

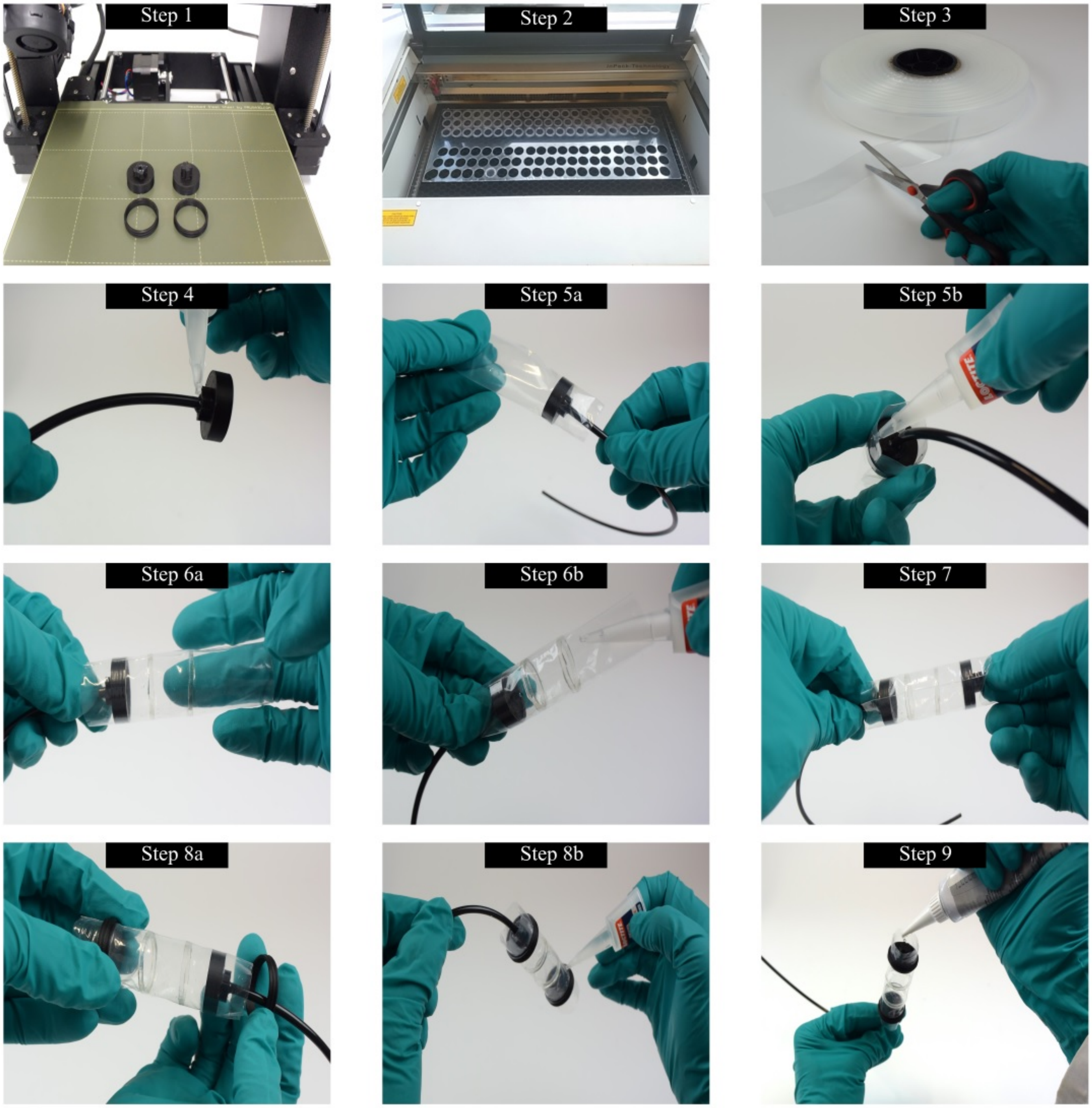

Fig. S1. Fabrication - Inner soft core. Snapshot of the nine steps required to fabricate and assemble the inner soft core.

Fig. S2. Fabrication - Metamaterial Sleeve. Snapshot of the three key steps involved in making the metamaterial sleeve functional.

S2. Experiments

This section explains our methods to obtain the metamaterial sleeve actuator's pressure-volume curve.

S2.1. Pressure - volume curve. To characterize the pressure-volume response of a metamaterial sleeve actuator, we fabricate it as described in S1, and connect it to the pressure-volume measuring setup. This setup performs a stepwise inflation of the inner soft core with a known volume and measures the resulting pressure in the softcore cavity. The volume within the actuator over time is monitored and recorded by a LabVIEW program running on a personal computer. This program controls a custom syringe pump, which consists of an Arduino Uno operating with the LabVIEW Interface for Arduino. The system includes a motor shield, a stepper motor (QSH-4218-35-10-027, Trinamic), a linear stage (LX-2001C, Misumi) and a gastight glass syringe (model 1050 TLL, Hamilton Company). Operating the stepper motor in half-stepping mode provides a volumetric resolution of 2.1 µL per step of the syringe pump. To ensure that the volume displaced by the syringe pump corresponds precisely to the increase in the soft core's volume, all tubing is rigid, and the entire fluidic circuit is filled with water. As the syringe pump determines the change in actuator volume, a piezoresistive pressure transducer (PR-21S, Keller Druckmesstechnik), powered by a DC voltage supply (E0300-0.1, Delta Elektronika), measures the pressure within the softcore. Finally, an analog data acquisition card (NI 9215, National Instruments) is used to transmit the pressure signal to the LabVIEW program with a resolution of 15.2 Pa. To eliminate the influence of gravity, we submerged the metamaterial actuator (water-filled) in a water tank (see Fig S3). A measurement of the metamaterial sleeve actuator is initiated through the LabVIEW program. During inflation, the pressure-volume curve of the inner soft core is shown in Fig S4).

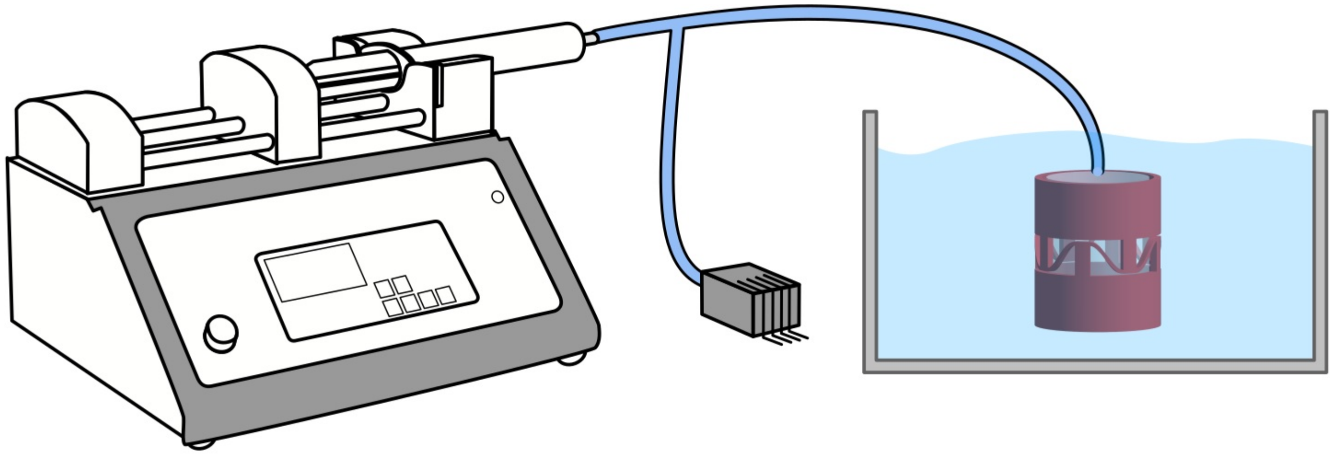

Fig. S3. Pressure-volume test setup. Schematic of the test setup used to characterize the pressure-volume curve of our metamaterial sleeve actuator.

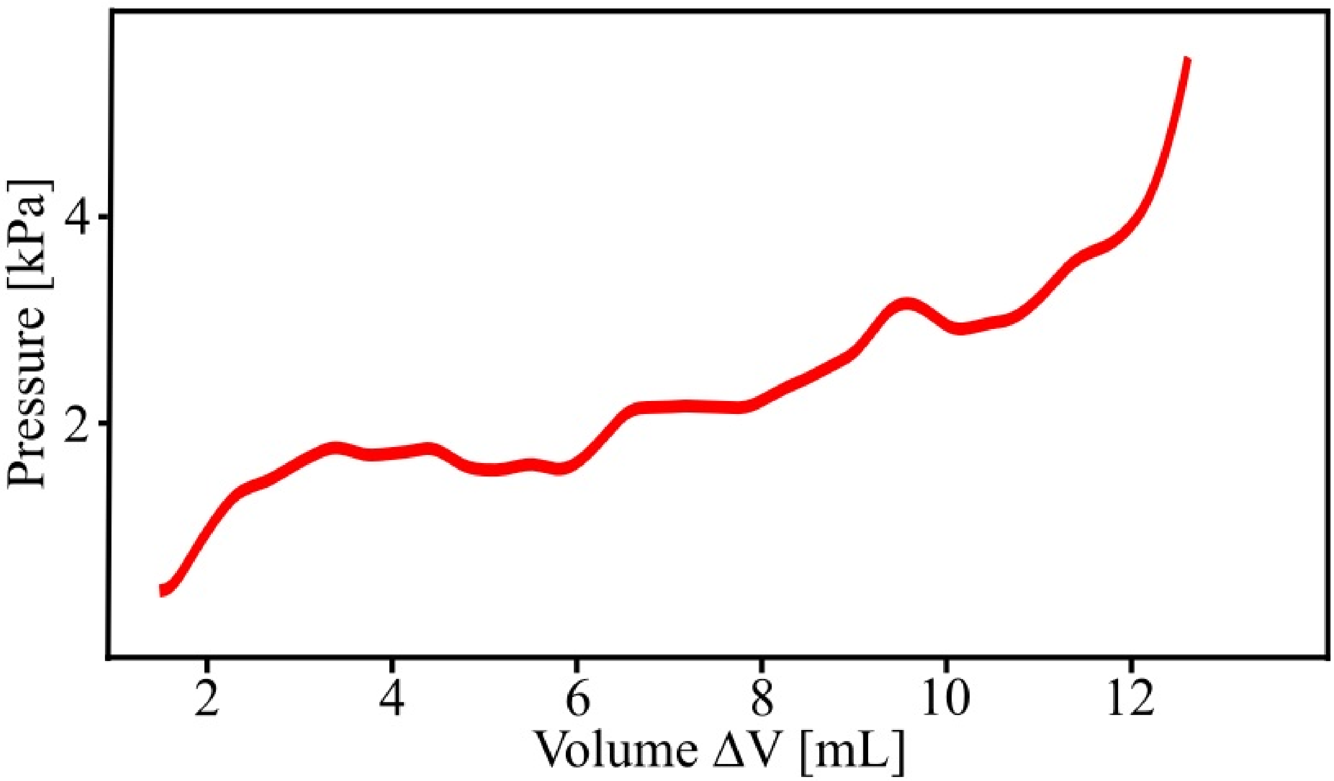

Fig. S4. Pressure-volume curve of the metamaterial sleeve actuator. A) Pressure-Volume (PV) curve of the inner soft core (membrane) during inflation.

S3. Modeling

In this section, we describe the simulations conducted to characterize the force-displacement response of a metamaterial unit cell.

S3.1. Metamaterial - Unit cell. We used finite element (FE) simulations in Abaqus (Abaqus/CAE 2022, Dassault) to model the behavior of a unit cell under displacement loading in combination with a Reference point (using coupling constraint). We used the Neo-Hookean material model with C10=1 Mpa and D1=0 in all simulations, to ease non-dimensionalisation. To dimensionalize the results, one can just multiple the nondimensionalized force by the initial shear modulus of the used material. As can be seen on Fig S5, the force initially increased during loading, then decreased slightly, exhibiting negative stiffness, before continuing to increase monotonically. The slender beams cause this snapping behavior; however, as the lower points of the slender beams move outward (away from the structure), the region exhibiting negative stiffness is limited. As this unit cell is designed to be combined with multiple unit cells, we incorporated the neighboring effect by connecting the left nodes of the unit cell to the right nodes (both node sets are highlighted in red). During loading, the force increases with displacement, followed by a plateau, and eventually enters a negative stiffness region characterized by a reverse slope. The side node sets of the unit cell push against each other, causing out-of-plane deformation of the slender beams. This behavior is reflected in the plateau, where the force increases slightly while displacement rises. In this configuration, the unit cell exhibits bistability. When the movement of the unit cell is restricted in the z-axis direction and the neighbor effect is also applied, a distinct peak and valley become clearly observable (see Fig S5).

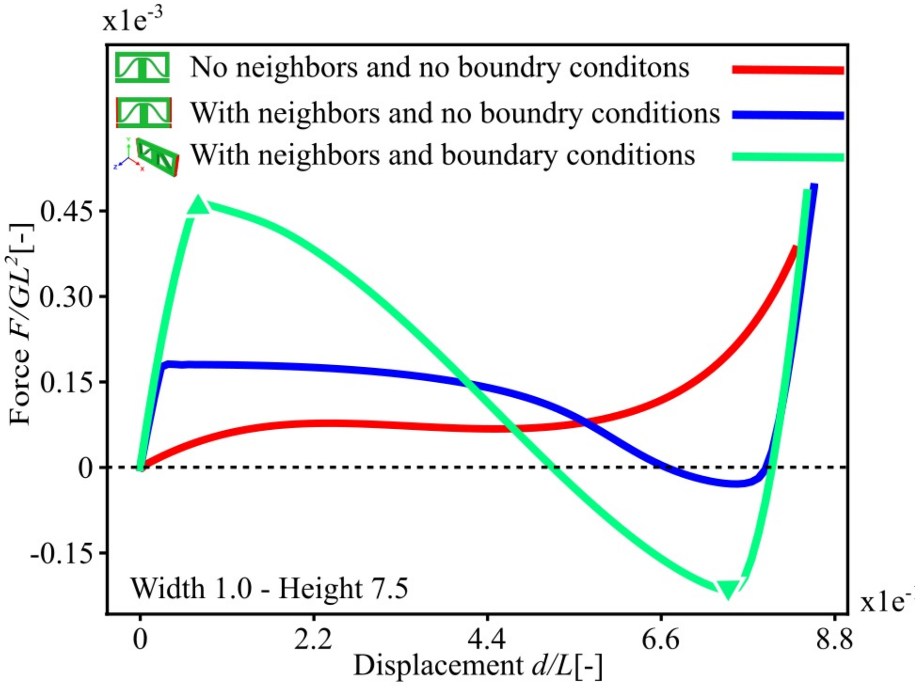

Fig. S5. Force-displacement response of a metamaterial unit cell under varying boundary conditions and the influence of neighboring effects.

S3.2. Metamaterial - Circular unit. During loading/unloading, the force-displacement curve of the symmetric and asymmetric metamaterial circular unit demonstrated two peaks and two valleys (Fig 3 and see Fig S6). We reported the numerical evolution of two peaks and two valley forces as a function of h/L and t/L for a circular unit subjected to an axial displacement D = 16 mm (see Fig S7).

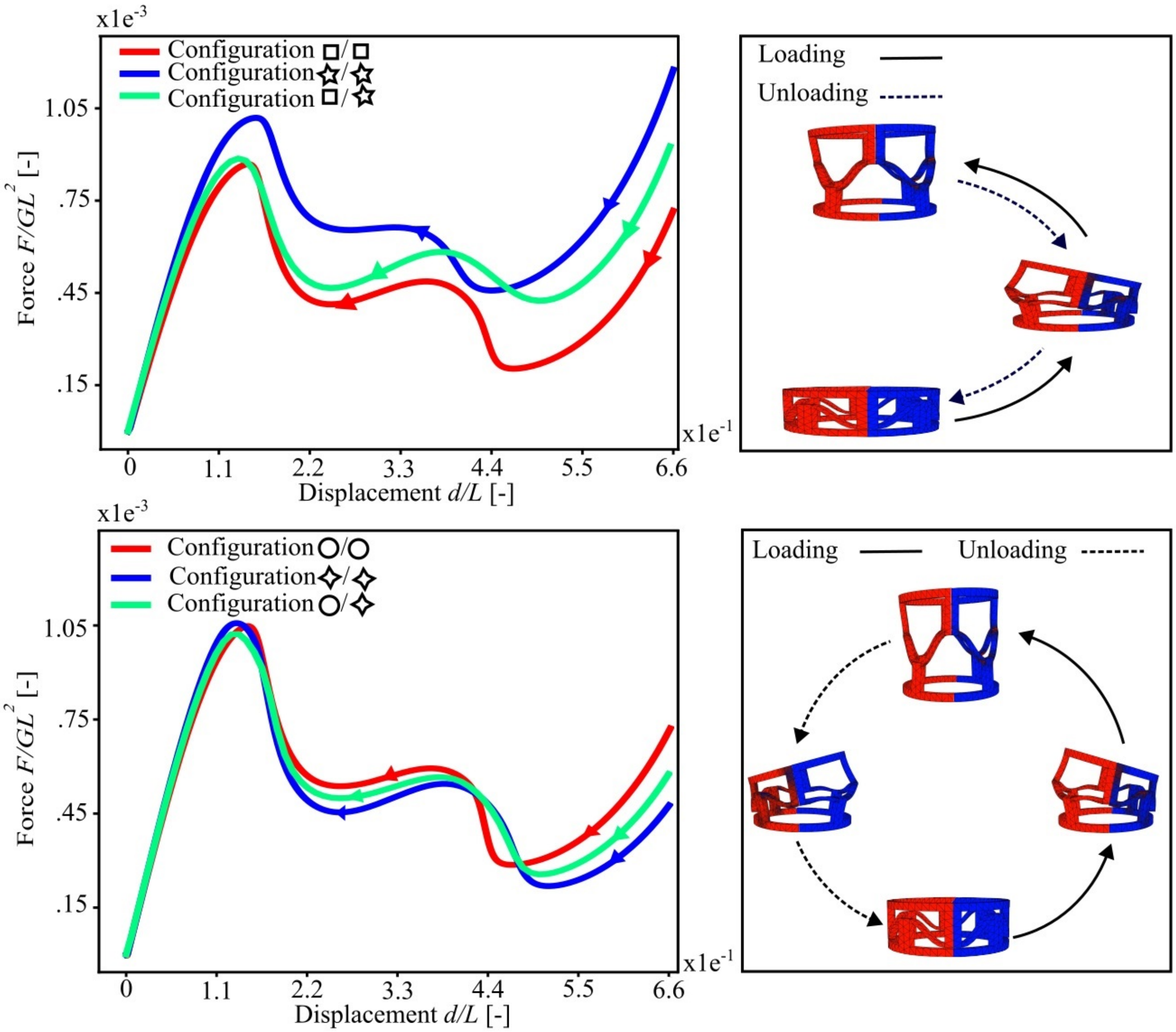

Fig. S6. A) Red and blue colors represent the FD relationship (during unloading) for combinations with ■ and ★ symbols, respectively. The green color symbolizes the merged circular unit from both combinations. The merged circular unit demonstrates symmetric sequencing during the loading/unloading cycle. B) Red and blue colors represent the FD relationship (during unloading) for combinations with ● and ✦ symbols, respectively. The green color symbolizes the merged circular unit from both combinations. The merged circular unit demonstrates asymmetric sequencing during the loading/unloading cycle.

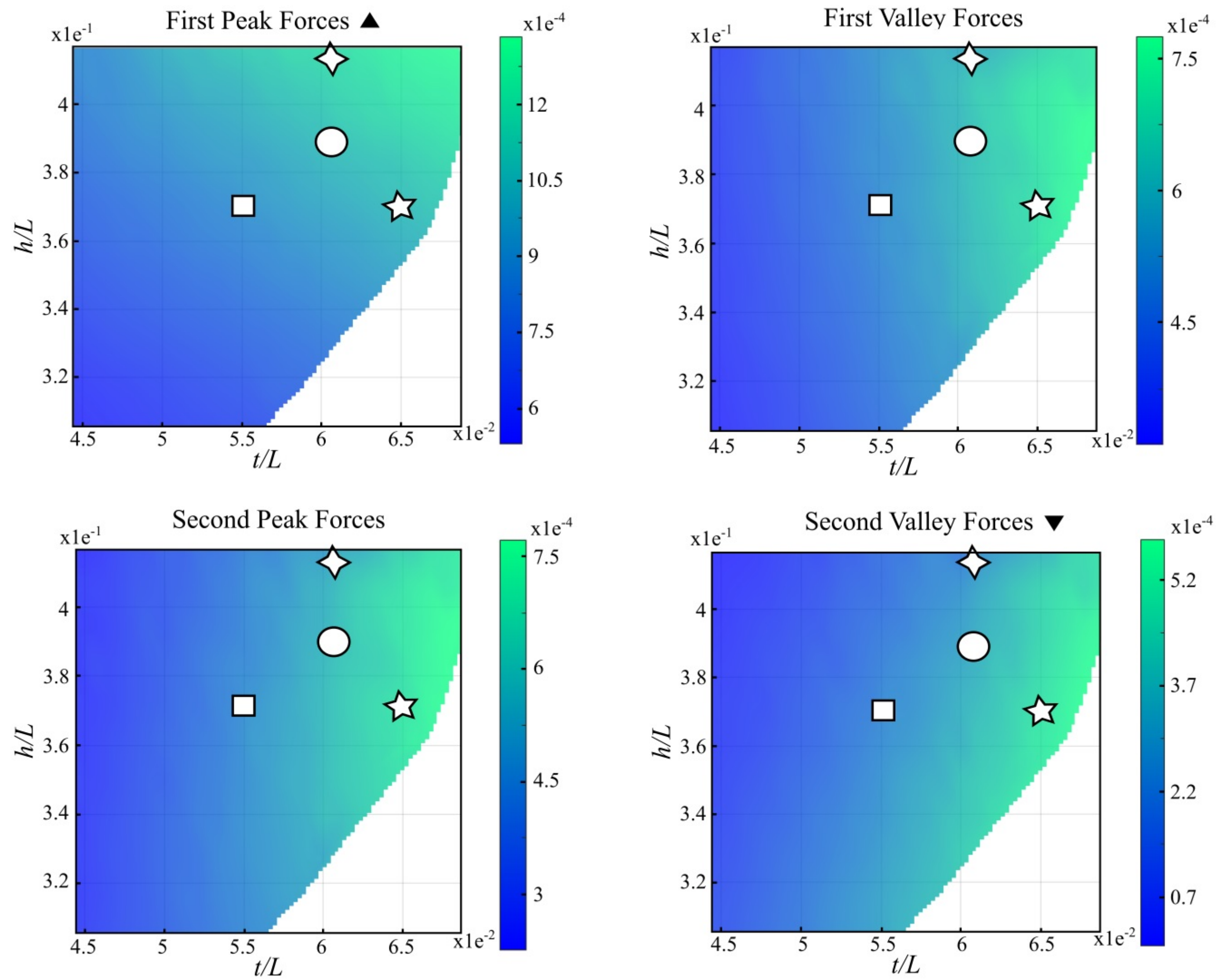

Fig. S7. Evolution of the first peak (P_1), first valley (V_1), second peak (P_2) and second valley (V_2) forces as a function of h/L and t/L for circular units.

S3.3. Metamaterial - Mesh refinement study. We present simulated results for cylindrical tessellated units with 1, 2, 3, and 4 elements in the cross-section of slender beams (see Fig S8). Mesh convergence is reached when the structure has more than 3 elements over the thickness, however this comes at the cost of computational power. A single simulation takes 55, 103, 318, and 732 minutes for design with respectively 1, 2, 3, and 4 elements over the thickness (simulations run on a intel i7 processor with 32 Gb of RAM). Notably, the time difference is significant compared to the variation in the FD curves. Therefore, for this study, we have selected a mesh size with a single element in the slender beam.

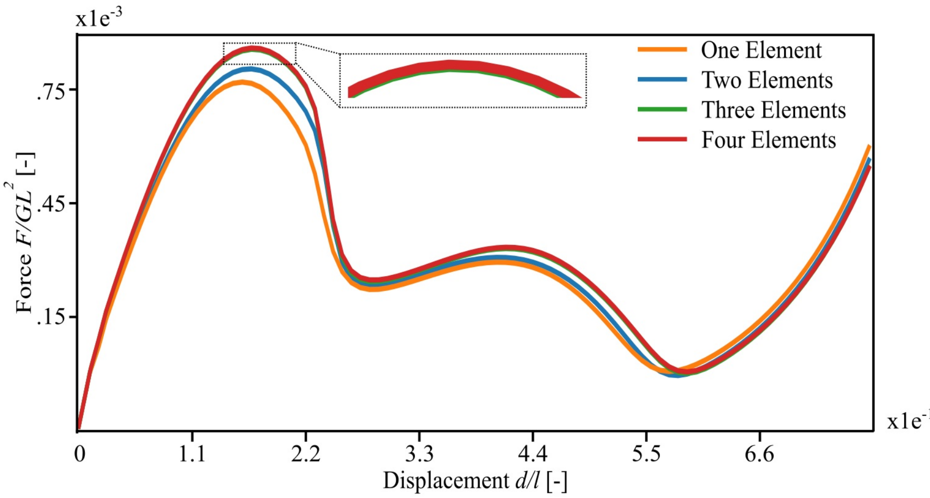

Fig. S8. Force displacement relationship Fd response of a same configuration with different meshing element sizes in the cross-section of slender beams

S4. Additonal Results

S4.1. Metamaterial - Multiple Unit Cells. We present simulated results with 8, 16 and 32 unit cells (see Fig S9). The results indicate that the first peak corresponds to the snapping of half of the unit cells in all three configurations, while the second peak represents the snapping of the remaining half, when only 2 or 3 unit cells are arranged along the circumference, we see that the second peak disappears, and off-axis symmetry breaking is also not present.

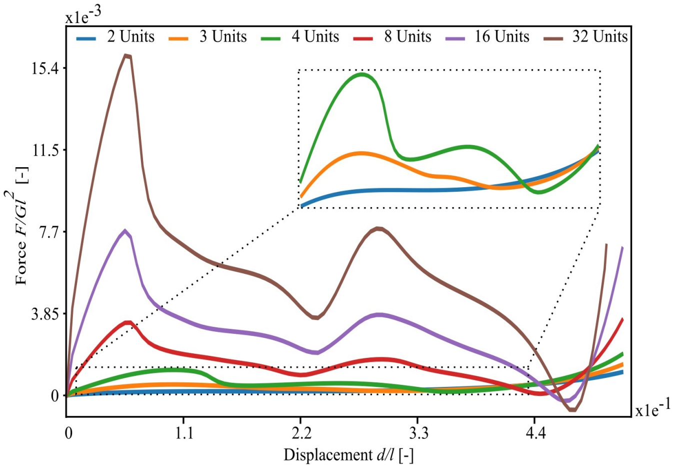

Fig. S9. Force Displacement relationship. FD response of multiple configurations with different unit cells in cylindrical tessellation.

S4.2. Strain Analysis. FEM analysis indicated that the maximum strain in the structure reaches approximately 47% (see Fig S10). This value is significantly lower than the yield strain of the Ultrasint Thermoplastic Polyurethane 90A-01 from Materialise, which has a reported elongation at break of 220%. Consequently, no material deterioration was observed during cyclic loading, demonstrating the material's durability under repeated use.

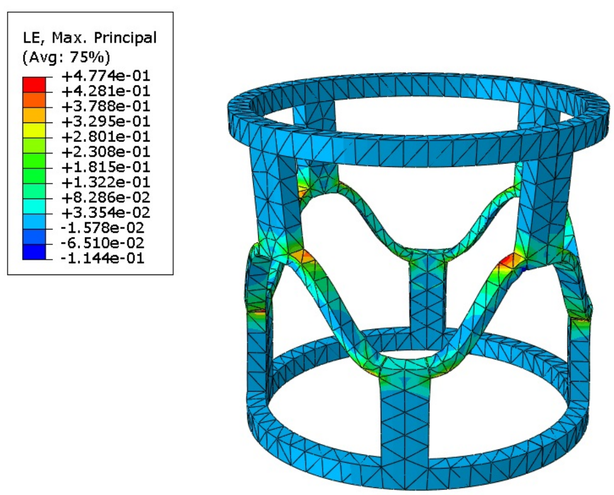

Fig. S10. Maximum stain analysis. Maximum strain observed in the slender beam elements during FEA.

Video S1. Simulation - Sequencing in metamaterial sleeve actuators The circular metamaterial ring units are loaded with displacement by the reference point (with coupling constraint). The merged circular unit form ■ and ★ set of combinations demonstrates symmetric sequencing during the loading/unloading cycle and the merged circular unit from ● and ✦ set of combinations demonstrates asymmetric sequencing during the loading/unloading cycle.

Video S2. Experimentation - Sequencing in metamaterial sleeve actuators To characterize the pressure-volume curve of the metamaterial sleeve actuators. Both types of actuators were tested with the pressure-volume setup. The symmetric metamaterial actuator clearly shows the same deformation pattern during the inflation/deflation cycles, however, the asymmetric metamaterial actuator followed a different deformation during the inflation/deflation cycle.

Video S3. Walking robot with metamaterial sleeve actuators on skateboard support A robot equipped with metamaterial sleeve actuators as legs walks with each inflation and deflation cycle. The metamaterial sleeve actuators sweep an area, aiding the robot's movement during walking on a skateboard support.

Video S4. Walking robot with metamaterial sleeve actuators without support A robot equipped with metamaterial sleeve actuators as legs walks with each inflation and deflation cycle. The metamaterial sleeve actuators sweep an area, aiding the robot's movement during walking even without support.